
Article:
Leiviskä, Miina, Jenkins, Sarah, Evans, Richard F.L. orcid.org/0000-0002-2378-8203 et al. (2 more authors) (2023) Local setting of spin textures in a granular antiferromagnet. Physical Review B. 184424. ISSN 2469-9969

https://doi.org/10.1103/PhysRevB.108.184424

Local setting of spin textures in a granular antiferromagnet

Miina Leiviskä [1,*] Sarah Jenkins [2] Richard F. L. Evans [2,†] Daria Gusakova [1] and Vincent Baltz [1,‡]
[1]*Univ. Grenoble Alpes, CNRS, CEA, Grenoble INP, IRIG-Spintec, F-38000 Grenoble, France*
[2]*School of Physics, Engineering and Technology, University of York, York YO10 5DD, United Kingdom*

(Received 14 February 2023; revised 11 August 2023; accepted 25 October 2023; published 22 November 2023)

Controlling the magnetic order of antiferromagnets is challenging due to their vanishing net magnetization. For this reason, the study of local spin textures in antiferromagnets is restricted by the difficulty in nucleating such states. Here, using atomistic simulations we demonstrate a method for nucleating localized spin textures in the grains of the thin-film antiferromagnet γ-$IrMn_3$. Utilizing the exchange bias coupling between a ferromagnet and an antiferromagnet, we set the spin texture in the latter from a predefined spin texture in the former by means of a thermal cycling procedure. The local textures set in the antiferromagnetic grains are shown to be stable against field perturbations. We also discuss how various material parameters affect the efficiency of the setting and the characteristics of these set textures. The setting of antiferromagnetic spin textures provides a potential route to antiferromagnetic spintronic devices with noncollinear spin states such as skyrmions, bubbles, and domain walls.

DOI: 10.1103/PhysRevB.108.184424

I. INTRODUCTION

The interest in antiferromagnetic (AFM) states is founded on their robustness against perturbations, such as magnetic fields, as well as on their physical properties that extend the potential of spintronics beyond that based on ferromagnets (FM) only [1,2]. Analogously to FMs, local spin textures with inhomogeneous magnetization configurations exist in AFMs under conditions yielding a favorable energy balance. Due to the different local symmetries, the expected properties of these AFM spin textures differ from and have interesting advantages over their ferromagnetic counterparts [3]. However, due to the lack of net magnetization, the main barrier to accessing these properties is the difficulty in experimentally nucleating them. Typically, structures with a size comparable to the critical single domain size or domain wall width are patterned to make the global multidomain structure of continuous films energetically unfavorable so that local spin textures form instead [4,5]. Alternative methods for the nucleation of local AFM spin textures have also been proposed: through injection of vertical spin-polarized current in nanostructured devices [6] or through subjecting the system to ultrafast laser pulses [7].

Here, we use atomistic simulations to demonstrate a local nucleation of spin textures in AFM grains that does not require complex device geometries and is applicable beyond metallic AFMs. Utilizing the exchange bias coupling at a FM/AFM interface and a thermal cycling procedure, we set the spin texture in the AFM grains during their magnetic ordering from predefined spin textures in the FM. This method follows previous experimental works on setting AFM domains and domain walls [8], vortices [4,5], and bubbles [9]. In this work, we nucleate prototypical spin textures, namely, skyrmion bubbles (Sk), in a continuous thin film FM using a carefully optimized magnetic stack and an external field. We then use this as a template for the setting of the underlying AFM grains, as shown in Fig. 1. Note, however, that the spin textures set in the AFM grains are not topologically protected despite the initial template comprising Sk bubbles.

II. THE SIMULATION SYSTEM

The simulation system $Ni_{80}Fe_{20}$ (0.87)/Co (0.33)/Pt (0.47)/γ-$IrMn_3$ (5 nm) is based on an experimental one that has been optimized for the nucleation of Sks in the FM layer [9,10]. The ultrathin Co/Pt bilayer provides a strong interfacial Dzyaloshinskii-Moriya interaction (DMI) [11] and some perpendicular magnetic surface anisotropy, while the thickness of the NiFe layer allows the vanishing of the total anisotropy. The magnetic coupling between the FM and AFM layers is preserved due to finite atomic intermixing. For the AFM layer we use the noncollinear γ-$IrMn_3$, due to its large exchange bias coupling originating from the statistical imbalance of spins in the four magnetic sublattices, which yields uncompensated interfacial spins [12]. Moreover, the four easy axes [13] of $IrMn_3$ may facilitate the magnetic moment winding that is necessary for a noncollinear spin texture formation. The magnetic properties of γ-$IrMn_3$ relating to its nontrivial spin structure have been thoroughly characterized using the atomistic simulation software package VAMPIRE [14,15], which is also used for this work. The simulations utilized the ARCHER2 supercomputer with typical simulations running on 1024 CPU cores due to the large number of Monte Carlo time steps and the large system size of around 6×10^6 spins.

*leiviska@fzu.cz
†richard.evans@york.ac.uk
‡vincent.baltz@cea.fr

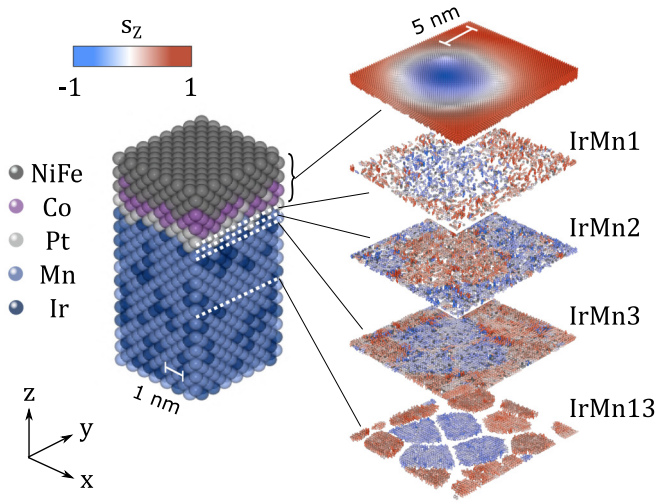

FIG. 1. (Left) Atomic structure of a slice of the simulation system consisting of a hybrid NiFe/Co/Pt FM single crystal coupled to a granular γ-IrMn$_3$ AFM across an atomically intermixed interface. The full size of the simulation system is $100 \times 100 \times 6.67$ nm^3. (Right) Cross section of the spin texture obtained in the FM and at several depths in the AFM, following a thermal cycling procedure. The numbers indicate the relative position of the AFM monolayers away from the interface.

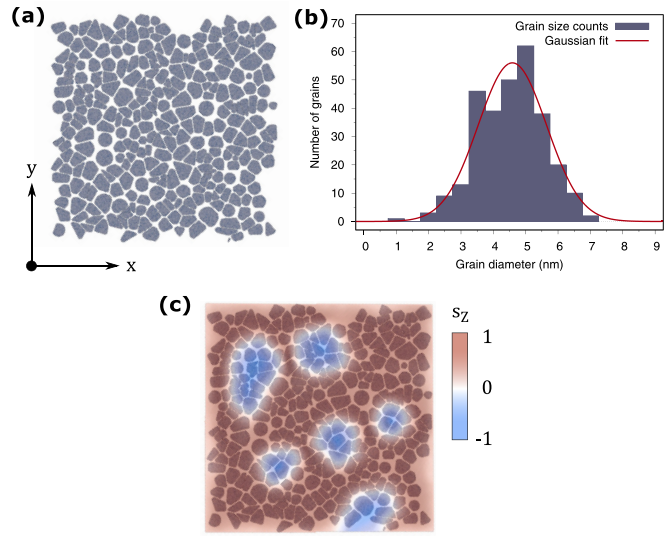

FIG. 2. (a) The bare grain structure of the AFM layer created using a Voronoi construction. (b) The grain size distribution showing an average grain size of ∼4.5 nm. (c) Overlaying the FM layer spin structure and the bare grain structure shows that the irregular shape of the skyrmions in the former follows the grain boundaries of the latter.

The spin Hamiltonian governing the energetics of the system is given by

$$\mathscr{H} = -\sum_{i<j} J_{ij}\mathbf{S}_i \cdot \mathbf{S}_j - \sum_{i<j}^{z} k_{\mathrm{N,i}}(\mathbf{S}_i \cdot \mathbf{e}_{ij})^2 - \sum_{i<j} \mathbf{D}_{ij} \cdot (\mathbf{S}_i \times \mathbf{S}_j) - \sum_i \mu_{s,i}\mathbf{S}_i \cdot \mathbf{B}_{\mathrm{ext}}. \quad (1)$$

The first term is the exchange interaction, where subscripts i and j refer to spins on sites i and j, J_{ij} is the exchange constant, and $\mathbf{S}_i$ is the spin vector. The second term describes the Néel pair anisotropy that rotates the spins radially/tangentially with respect to a nearest neighbor of a given element and is used to simulate the interfacial perpendicular magnetic anisotropy (Co spins point radially to Pt sites) and correct anisotropy of IrMn$_3$ (Mn spins point tangentially to Ir sites) [13]. Here, $k_{\mathrm{N,i}}$ is the Néel pair anisotropy constant, $\mathbf{e}_{ij}$ is a unit vector between atoms i and j, and z is the number of nearest neighbors. The third term that stabilizes the topological states is the DMI interaction where $\mathbf{D}_{ij}$ is the DMI vector, defined as $\mathbf{D}_{ij} = D_{ij}(\hat{\mathbf{r}}_{ik} \times \hat{\mathbf{r}}_{jk})$, where D_{ij} is the DMI strength and $\hat{\mathbf{r}}_{ik,jk}$ is the unit vector between the magnetic atoms at site i and j and Pt at site k. The fourth term is the Zeeman energy where $\mu_{s,i}$ is the atomic magnetic moment and $\mathbf{B}_{\mathrm{ext}}$ is the external induction or flux density. For the sake of computational simplicity, we have not included the Ruderman-Kittel-Kasuya-Yosida (RKKY) interaction, which would increase the exchange interaction strength between the FM and AFM layers but not change the physics of the local setting presented in this work.

The temperature dependence of the magnetic state is simulated using an adaptive Monte Carlo Metropolis algorithm [16], which is ideal for naturally simulating the temperature evolution of the magnetic state. The field dependence, on the other hand, was simulated using the stochastic Landau-Lifshitz-Gilbert equation and a Heun numerical scheme [17]. We have set the damping parameter to 1 to promote rapid relaxation and therefore faster numerical calculation, since our goal is to reach the ground state rather than follow the exact dynamics. The time step is 0.1 fs.

The simulation system with a size of $100 \times 100 \times 6.67$ nm^3 has a layer-dependent structure: the FM/Pt multilayer is a single crystal, while the AFM layer is granular with an average grain size and spacing of ∼4.5 and 0.75 nm, respectively, in line with experimental data [18]. Similarly to an experimental system, the AFM grains are not coupled to each other [19]. On the other hand, the FM grains are coupled and as the FM and AFM grains are coincident, the FM layer can be modeled as a single crystal. The grain structure (illustrated in Fig. 2) is created using a Voronoi construction as described previously in Ref. [20]. It should be noted that we have not implemented periodic boundary conditions as they are incompatible with the implementation of the AFM grain structure. The crystal orientation of the entire simulation stack is such that the [001] crystal axis is along the film normal.

The on-site magnetic properties of each magnetic element in the simulation stack are listed in Table I. For the

TABLE I. Parameters used in the simulation for each magnetic element.

Parameter	$Ni_{80}Fe_{20}$	Co	Mn
μ_s (μ_B)	1.05	1.72	2.6
$k_{\mathrm{N}}(10^{-22}$ J/atom)	–	0.025 (Pt)	−4.22 (Ir)
Intermixing (Å)	1.67	1.67	3.34

TABLE II. Matrix of exchange (J_{ij}) and DMI* coefficients (D_{ij})(10^{-21} J/link) for the interactions between the different elements in the stack. NN stands for nearest neighbors and NNN for next-nearest neighbors.

	NiFe	Co	Pt	Mn
NiFe	3.8 [15]	5	0.5*	1.21 [21]
Co	5	6.1 [15]	0.5*	1.21 [21]
Pt	0.5*	0.5*	–	–
Mn	1.21 [21]	1.21 [21]	–	−6.4 (NN) [21] 5.1 (NNN) [21]

permalloy layer ($Ni_{80}Fe_{20}$), μ_s was calculated from the saturation magnetization M_s of $\sim 8.6 \times 10^5$ A/m using $\mu_s = M_s a^3/n_{at}$ [15], where a is the lattice constant and n_{at} is the number of atoms in the unit cell. For Co the values were obtained from Ref. [15] and for γ-$IrMn_3$ they were obtained from Ref. [12]. The intermixing in Table I refers to the thickness over which the given layer is intermixed with the one below. The intersite exchange (J_{ij}) and the DMI (D_{ij}) interactions are listed in Table II. For $Ni_{80}Fe_{20}$ the J_{ij} is calculated from the expected Curie temperature T_c of ∼900 K using $J_{ij} = 3k_B T_c/\epsilon z$, where $\epsilon = 0.79$ is the spin-wave mean-field correction and z is the number of nearest neighbors [15]. For Co the values are obtained from Ref. [15] and for γ-$IrMn_3$ they are obtained from *ab initio* calculations [21]. For the coupling strength between Co and NiFe, we have used the average Co-Co and NiFe-NiFe coupling strengths. The DMI value used in our calculations is 0.5×10^{-21} J/link, which corresponds to the interfacial DMI parameter $D_s = 0.5$ pJ/m for the limiting case of a flat interface. Experimental values available in the literature for similar stacks (measured by Brillouin light scattering) range from ∼0.15 to ∼1.25 pJ/m [9,22,23]. We have verified that varying the DMI value within this range does not alter the main conclusions of the paper.

III. LOCAL SETTING OF THE AFM GRAINS

The localized setting of the AFM grains is realized by means of thermal cycling. More precisely, the simulations were carried out in three steps: (i) FM Sk nucleation, (ii) field-cooling, and (iii) field removal. During the first step [Figs. 3(b)–3(d)], the system was equilibrated at 600 K in an applied field of $B_z = 0.5$ T parallel to the film normal for 10^6 Monte Carlo steps. Because 600 K is above the Néel temperature (T_N) of the AFM layer [∼510 K, see Fig. 3(a)] and below the Curie temperature of the FM layer [∼900 K, see Fig. 3(a)], this phase allows the nucleation of nanoscale Sks in the FM layer while the AFM layer remains disordered throughout. This ensures that the setting of spin textures is from the FM to the AFM layer and not vice versa. In the second simulation step [Figs. 3(e)–3(g)], the system is cooled down to 0 K in the same field in order to further stabilize the FM layer and to set the AFM layer upon crossing the Néel temperature T_N. The bulk AFM (exemplified by IrMn layer 13 in Fig. 3) begins to set at the blocking temperature of the IrMn grains around $T \approx 500$ K. The interfacial moments of the AFM (IrMn 1 in Fig. 3), on the other hand, are subject to more thermal noise and the setting of the AFM spin textures is more difficult

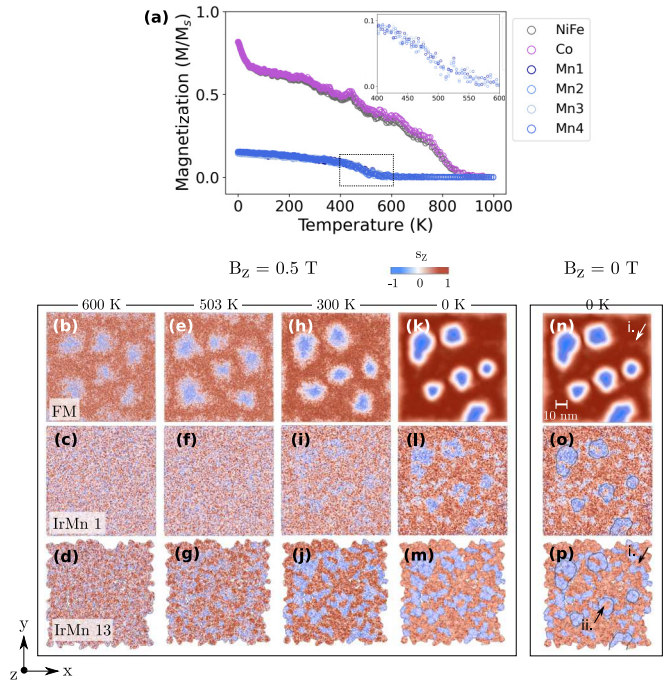

FIG. 3. (a) Temperature dependence of the magnetization (M/M_s) of each magnetic material in the simulation stack. (b)–(m) Top view snapshots of the evolution of the spin textures in the FM (top row), the AFM at the interface (middle row, IrMn 1), and the AFM in the core (bottom row, IrMn 13), under out-of-plane field cooling ($B_z = 0.5$ T): at 600 K, above the Néel temperature T_N of the AFM; at 503 K, near T_N; at room temperature; and 0 K well below T_N. (n)–(p) The spin textures at remanence, for $B_z = 0$ T. The contours of the FM textures in panel (n) are superimposed to panels (o) and (p), as visual guides.

to discern. This is likely due to the reversible component fluctuating with the FM spins. At $T = 0$ K [Figs. 3(k)–3(m)], the setting of the AFM interface and bulk based on the FM spin textures becomes clear: the textures observed in the FM are largely reproduced in the bulk AFM as highlighted by the contours in Figs. 3(o) and 3(p) and their exact shape is governed by the grain boundaries of the AFM.

Superimposed to the set spin textures there are also random spin textures in the AFM bulk that do not correspond to the FM spin configuration. These discrepancies can be divided into two categories based on their location and the extent of deviation: discrepancies exemplified by "i." in Figs. 3(n) and 3(p) are in the region of uniformly magnetized FM and often accompanied by slight impressions in the adjacent FM layer. Discrepancies exemplified by "ii." in Fig. 3(p) are inside the imprinted spin textures and deviate completely from the FM spin configuration. The reason for these discrepancies is likely due to the FM-AFM exchange interaction not being strong enough to set all the grains, which is demonstrated in Fig. 4(a)—stronger exchange interaction improves the FM-AFM spin texture conformity, while zero exchange interaction results in the AFM having a completely random domain structure. A similar outcome is realized when the intermixing at the Pt/AFM interface is increased, as shown in Fig. 4(b) because more FM and AFM spins will come to a direct

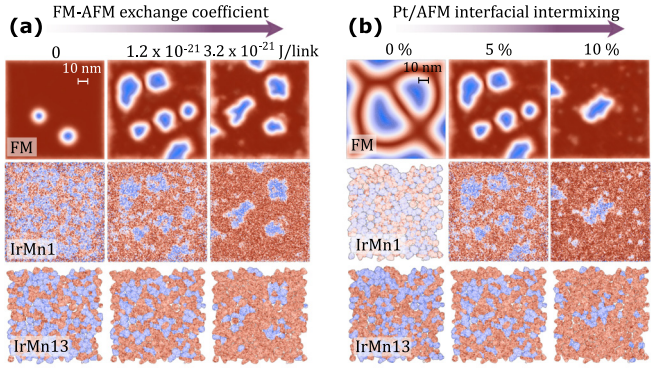

FIG. 4. The effect of increasing (a) the exchange coefficient strength and (b) the intermixing between the Pt and AFM layers on the imprinting efficiency in terms of FM-AFM spin texture conformity and absence of discrepancies.

contact, which facilitates the AFM-FM exchange interaction. We recall that for the sake of computational simplicity we have not included the RKKY interaction. This would increase the exchange interaction strength between the FM and AFM layers and give rise to nonzero exchange bias in the absence of intermixing but not change the physics of the local setting presented in this work. It is also possible that some of the "i." type discrepancies are residual imprintings of FM Sks that moved or were annihilated during the field-cooling [compare the FM Sk locations in Figs. 3(b) and 3(n)]. We also point out that layer intermixing is likely to finely modify some magnetic properties [24] and parameters like DMI, which can also alter the imprinting efficiency.

Finally, the last simulation step shown in Figs. 3(n)–3(p) is the removal of the external field, which causes only minor changes to the spin textures throughout the stack, demonstrating the zero-field stability of the set localized AFM spin textures.

In summary, this set of simulations shows that (i) spin textures (here Sks) initially nucleated in a FM layer serve as a template for the localized setting of spin textures in the AFM grains during a thermal cycling protocol, (ii) the setting of the AFM textures penetrates into the bulk of the AFM, and (iii) the AFM textures are stable at remanence. Note that these conclusions are valid for any final temperature below T_N, including room temperature in our case [see Figs. 3(h)–3(j)]. The robustness and universality of our results is later further demonstrated in Fig. 8(b) where we show the setting of the AFM grains based on another FM spin texture, namely, maze domains.

IV. MICROSCOPIC DETAILS OF THE LOCAL SETTING

The exact nature and morphology of the set textures (Fig. 5) is discussed next. The radii of the Sks in the FM [Figs. 5(a)–5(b)] range from ∼10 to 20 nm and their shape is rather irregular, most likely due to the pinning by the grain boundaries of the AFM layer [see Fig. 2(c) for the conformity between the Sk shapes and the AFM grain structure].

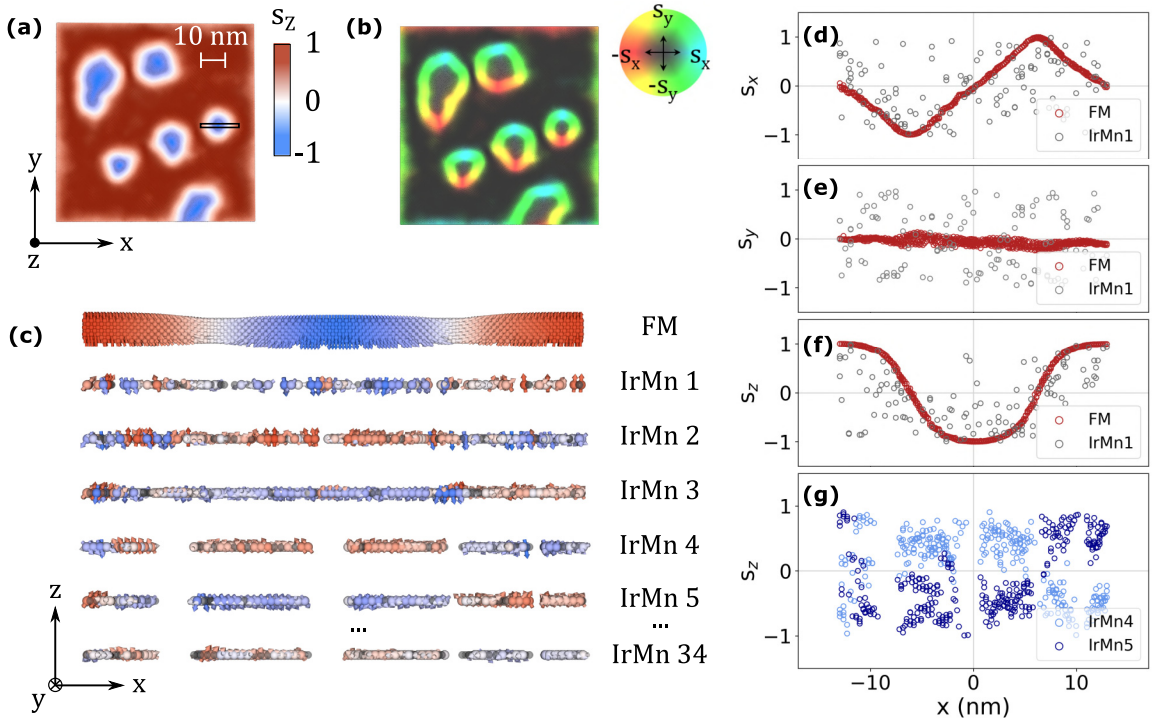

FIG. 5. Top view of the spin structure in the FM layer showing azimuthal (a) and rotational (b) components of the magnetization showing the existence of Sk bubbles in the ferromagnetic layer. (c) Layer-by-layer spin structure through the sample, corresponding to the cross section indicated in panel (a) showing the propagation of the spin texture into the antiferromagnet. The spin direction alternates in the alternating AFM monolayers due to the antiferromagnetic coupling. (d)–(g) Lateral dependencies of the spin components s_i in the FM, IrMn 1, IrMn 4, and IrMn 5 layers showing the presence of domain walls in the FM and corresponding structure in the antiferromagnet.

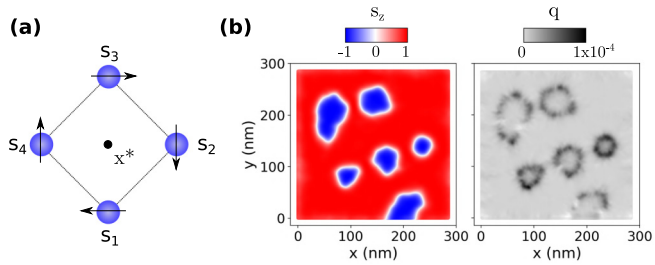

FIG. 6. (a) Schematic showing the method for calculating the topological charge density q of a discrete lattice made up of square unit cells. The total topological charge Q is the sum of q over the entire lattice. (b) The topological charge density calculated for the FM layer.

The variation of the spin components s_x, s_y, and s_z across the cross section shows behavior characteristic of a Néel-type Sk [Figs. 5(d)–5(f)], which is in good agreement with the interfacial DMI, and its strength being above the critical strength for a Bloch to Néel domain wall transition ($D_c = 4\mu_0 M_s^2 t \ln 2/2\pi^2$). The s_x and s_z components can be fitted using $\cosh^{-1}(\pi[x - x_0]/\Delta)$ and $\tanh(\pi[x - x_0]/\Delta)$ functions, respectively, where x_0 is the domain wall center location and Δ is the domain wall width. For the selected skyrmion, $\Delta \sim 8.4$ nm, which is in the same order of magnitude as expected by theory [25].

We calculate the winding number Q for our discretized system by summing up the topological charge density q per a square cell illustrated in Fig. 6(a):

$$q(x^*) = \frac{1}{4\pi}[(\sigma A)(s_1, s_2, s_3) + (\sigma A)(s_1, s_3, s_4)], \quad (2)$$

$$\sigma A(s_j, s_k, s_l) = 2\tan^{-1}\left(\frac{\mathbf{s}_j \cdot \mathbf{s}_k \times \mathbf{s}_l}{1 + \mathbf{s}_j \cdot \mathbf{s}_k + \mathbf{s}_j \cdot \mathbf{s}_l + \mathbf{s}_k \cdot \mathbf{s}_l}\right), \quad (3)$$

where σA is the signed area of a triangle delimited by $\mathbf{s}_j$, $\mathbf{s}_k$, and $\mathbf{s}_l$, and $\mathbf{s}_i$ is the magnetization vector at site i [26,27]. Figure 6 shows the calculation of the winding number for the FM layer in Fig. 3(n), which yields $Q = 1$ for each Sk bubble, confirming their topological nature. It should be noted that the FM spin texture at the boundary of the simulation system is not a Sk bubble (noninteger $Q \sim 0.4$) and thus is not topologically protected. Considering that the sum of the topological charge over the whole lattice should return an integer, the winding number of 0.4 of the FM texture should be compensated elsewhere. As the topological charge is only being calculated for the FM layer, it is possible that the AFM spins compensate the fractional Q or, alternatively, the existence of the boundary and pinning from the AFM may cause the fractional Q as technically Q is only defined for infinite systems.

At the AFM interface (IrMn 1 in Fig. 5), the s_x, s_y, and s_z components show average behavior that corresponds to that of the FM layer, providing further support for the AFM spin texture setting from the FM template. The increased noise is likely due to the strong anisotropy of γ-$IrMn_3$, the interfacial intermixing, and the interfacial magnetization comprising a reversible and an irreversible component [12,28], where the former follows the FM spins while the latter is strongly coupled to the AFM bulk. The different behaviors of these two components are also observed during the field cycling as is discussed later. In the AFM layer, the spin texture setting propagates from the topmost layer down to the bottom layer with the polarity of the texture alternating between each consecutive monolayer, as is shown in Fig. 1. This is in a good agreement with the typical tetrahedral $3Q$ spin state of the AFM ordering of γ-$IrMn_3$ [29] and [001] crystal ordering. To further confirm the alternating magnetization in the antiferromagnet we calculate the partial spin-spin correlation function between one layer of the ferromagnet and each layer of the antiferromagnet, shown in Fig. 7. The spin-spin correlation function is given by

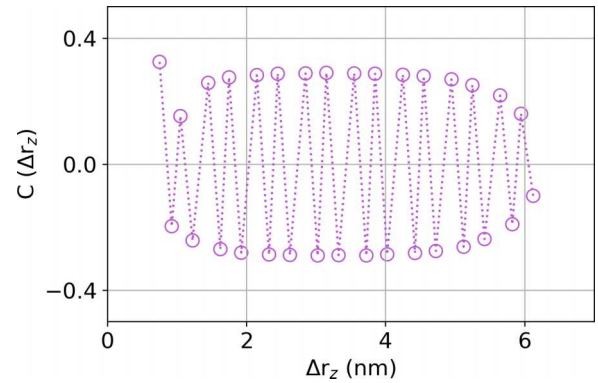

FIG. 7. Partial spin-spin correlation function of the spin texture showing alternating correlation in the s_z spin components between the ferromagnet and the antiferromagnet.

$$C(\Delta r_z) = \frac{1}{N}\sum_{i,j} s_i^z(r_z) s_j^z(r_z + \Delta r_z), \quad (4)$$

where i's are atoms in the center ferromagnetic layer (containing the ferromagnetic spin texture), j's are atoms in the antiferromagnet separated by a position vector r_z with z components only (we do not consider pairs of atoms separated laterally), and N is the total number of pairs considered. This gives the correlation between the ferromagnet and successive layers of the antiferromagnet, with a value of 1 being full correlation and -1 being fully anticorrelated. In the case of the spin texture, the ordering of the interfacial moments of the AFM is highly correlated with the ferromagnetic order, leading to a net and an alternating correlation between the FM and each layer of the AFM in the system. In the absence of FM-AFM coupling there is no net correlation and in the case of no spin texture the correlation is similar. The interfacial layer feels a strong exchange field from the ferromagnet leading to a large positive correlation, while the next two subsurface layers suffer frustration due to the intermixing with the ferromagnetic atoms. The bulk correlation is approximately constant but with a small decrease in the strength of correlation towards the bottom of the antiferromagnetic layer due to the loss of surface exchange bonds and a local decrease in antiferromagnetic surface order, in agreement with expectations [30–32].

In the bulk of the AFM (IrMn 13 in Fig. 5) the noise is reduced, as there is no need to accommodate intermixing and the resulting non-IrMn AFM bonds, but some noise remains from the local nature of the anisotropy of γ-$IrMn_3$ [13].

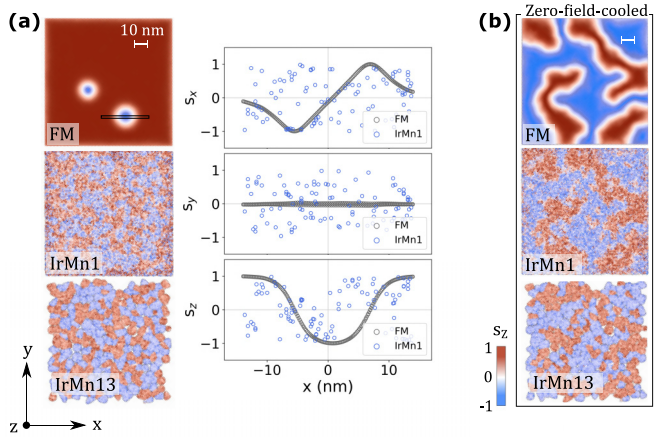

FIG. 8. (a) No imprinting is observed for a simulation system without exchange interaction across the FM/AFM interface. (b) Maze domains can be imprinted from the FM layer into the AFM layer under zero-field-cooling conditions.

The behavior of the s_z component follows that of the FM layer, with the only exception being that the domain walls are narrower as they follow the AFM grain boundaries. The penetration depth of the setting, down to the last layer IrMn 34 which is 5 nm away from the interface, is in good agreement with experimental reports of vortices in CoO and NiO [5] and exchange springs in γ-$IrMn_3$ [33], which could propagate over the whole AFM thickness. As a control simulation, in Fig. 8(a) we show that for a system without FM-AFM interfacial exchange coupling there is no correspondence between s_i of the FM and AFM layers and instead the setting of the AFM grains is random.

V. FIELD STABILITY OF THE SET AF GRAINS

Next, we study the effect of cycling the external field (oriented along the film normal) on the spin textures throughout the simulation stack. As expected, the hysteresis loop [Fig. 9(a)] shows a shift of ~ -0.7 T towards negative fields due to the exchange bias from the uncompensated, irreversible interfacial Mn spins [12]. The spin texture evolution, on the other hand, strongly depends on the layer. The FM layer follows the field, nearly saturating at strong fields [Figs. 9(b) and 9(d)] and gradually reversing at intermediate fields by the expansion of Sk bubbles. The AFM bulk, on the other hand, is unchanged throughout the field cycle as seen in Figs. 9(j)–9(m). This can also be seen in the fact that, at remanence, the FM layer [Figs. 9(c) and 9(e)] adopts a configuration that conforms with that of the AFM layer. The AFM interface comprises a reversible component that follows the FM and an irreversible component that abides by the AFM bulk and therefore shows a behavior that is a mixture of the two [Figs. 9(f)–9(l)]. This shows that the local spin textures that have been set remain unaltered in the AFM bulk and partially at the interface even after the original Sks in the FM layer are annihilated. This means that we can transform a system with Sks in the FM layer and no spin textures in the AFM [Figs. 3(a)–3(c)] to a system with no Sk in the FM layer but predefined spin textures in the AFM layer [Figs. 9(d)–9(l)]

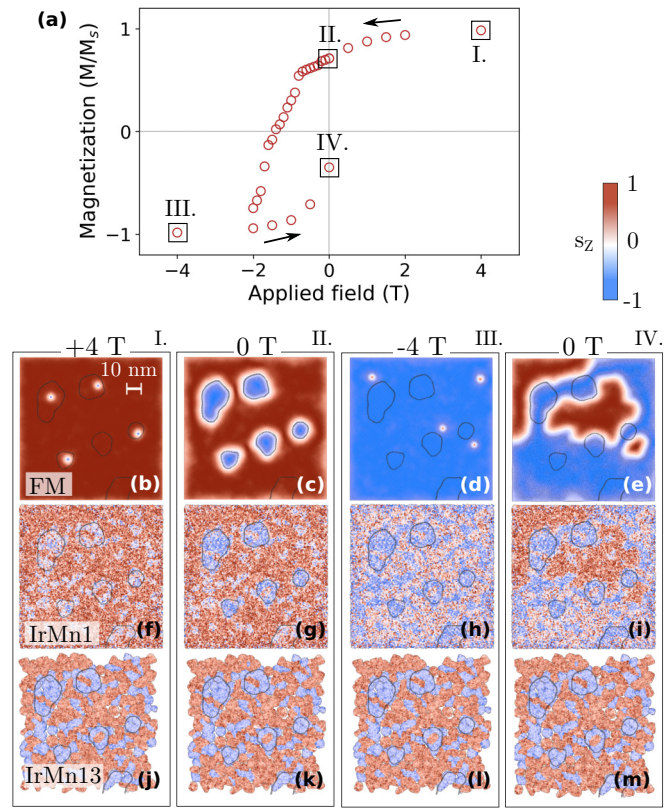

FIG. 9. (a) Field dependence of the FM magnetization (M/M_s) at 0 K and (b)–(m) snapshots of the evolution of the spin structures during the field sweep, in the FM (b)–(e), in the AFM at the interface [(f)–(i), IrMn 1], and in the AFM in the core [(j)–(m), IrMn 13]. The snapshots are taken at positive saturation (I.), forward remanence (II.), negative saturation (III.), and backward remanence (IV.). The contours of the FM Sks in Fig. 3(n) are superimposed to all images as visual guides.

using consecutive thermal and field cycling processes. This opens up perspectives for further studies of spintronic properties of isolated, localized spin textures in an AFM.

VI. DISCUSSION

Here we open the discussion on future study of topologically protected states in the real space of compensated magnets as they hold promise of favorable and technologically relevant properties [1,2,34]. These spin textures cannot be continuously transformed into a topologically trivial state and therefore are remarkably stable. Moreover, they impact the physical properties of the system as the winding of the spins allows the electrons to acquire a nonzero geometric phase [35,36] when interacting with the local spin structure. While our work demonstrates the localized setting of nontopological spin textures in AFM grains, the technique we have presented could be applied and optimized for continuous films of AFMs or compensated magnets with spin-split band structure [37,38]. The latter group is interesting due to their novel transport phenomena such as the spontaneous anomalous Hall effect [39–41] and spin current generation [42–44] allowed by the novel band topologies. A particular topological state of interest would be Sks with compensated magnetic ordering.

Due to the antiparallel interatomic exchange interactions they have not only zero net magnetization but also zero topological charge, which ensures robustness against external fields and vanishing skyrmion [6,45] and topological Hall effects [46]. Other predicted effects of AFM Sks on the transport properties include the nonvanishing topological spin Hall effect [46,47] and a longitudinal Sk velocity exceeding that of the FM Sks [6,45]. These properties make Sks with compensated magnetic ordering not only fascinating subjects for studies on topology but also competitive information carrier candidates for ultradense, ultrafast, low-power spintronic devices.

VII. CONCLUSION

In conclusion, we have theoretically demonstrated the setting of localized spin textures in antiferromagnetic γ-$IrMn_3$ by using predefined spin textures in an adjacent exchange-coupled ferromagnet as a template. This setting of nontopological spin textures was realized by a thermal cycling procedure and it was shown to extend beyond the interface through the entire thickness of the antiferromagnet (here 5 nm). The set AFM textures showed remarkable stability against field perturbations, and the setting efficiency and the morphologies of the set AFM textures were shown to depend on various material parameters. This work offers a solution for overcoming the challenge of nucleating localized real-space spin textures in compensated magnets with zero net magnetization, promoting the extension of local spin texture studies beyond ferromagnets.

ACKNOWLEDGMENTS

This study was partially supported by the France-U.K. Alliance Hubert Curien program (PHC) (Grant No. 46298XC) and the U.K. EPSRC program (Grant No. EP/V007211/1). This work used the ARCHER2 UK National Supercomputing Service [48]. Derived data supporting the findings of this study are available from the corresponding authors on request.

[1] T. Jungwirth, X. Marti, P. Wadley, and J. Wunderlich, Antiferromagnetic spintronics, Nat. Nanotechnol. **11**, 231 (2016).
[2] V. Baltz, A. Manchon, M. Tsoi, T. Moriyama, T. Ono, and Y. Tserkovnyak, Antiferromagnetic spintronics, Rev. Mod. Phys. **90**, 015005 (2018).
[3] O. Gomonay, V. Baltz, A. Brataas, and Y. Tserkovnyak, Antiferromagnetic spin textures and dynamics, Nat. Phys. **14**, 213 (2018).
[4] G. Salazar-Alvarez, J. J. Kavich, J. Sort, A. Mugarza, S. Stepanow, A. Potenza, H. Marchetto, S. S. Dhesi, V. Baltz, B. Dieny, A. Weber, L. J. Heyderman, J. Nogués, and P. Gambardella, Direct evidence of imprinted vortex states in the antiferromagnet of exchange biased microdisks, Appl. Phys. Lett. **95**, 012510 (2009).
[5] J. Wu, D. Carlton, J. S. Park, Y. Meng, E. Arenholz, A. Doran, A. T. Young, A. Scholl, C. Hwang, H. W. Zhao, J. Bokor, and Z. Q. Qiu, Direct observation of imprinted antiferromagnetic vortex states in CoO/Fe/Ag(001) discs, Nat. Phys. **7**, 303 (2011).
[6] X. Zhang, Y. Zhou, and M. Ezawa, Antiferromagnetic skyrmion: Stability, creation and manipulation, Sci. Rep. **6**, 24795 (2016).
[7] R. Khoshlahni, A. Qaiumzadeh, A. Bergman, and A. Brataas, Ultrafast generation and dynamics of isolated skyrmions in antiferromagnetic insulators, Phys. Rev. B **99**, 054423 (2019).
[8] G. Vallejo-Fernandez, T. Deakin, K. O'Grady, S. Oh, Q. Leng, and M. Pakala, Measurement of the antiferromagnet activity in exchange bias systems, J. Appl. Phys. **107**, 09D709 (2010).
[9] K. G. Rana, R. L. Seeger, S. Ruiz-Gómez, R. Juge, Q. Zhang, K. Bairagi, V. T. Pham, M. Belmeguenai, S. Auffret, M. Foerster, L. Aballe, G. Gaudin, V. Baltz, and O. Boulle, Imprint from ferromagnetic skyrmions in an antiferromagnet via exchange bias, Appl. Phys. Lett. **119**, 192407 (2021).
[10] O. Boulle, J. Vogel, H. Yang, S. Pizzini, D. de Souza Chaves, A. Locatelli, T. O. Menteş, A. Sala, L. D. Buda-Prejbeanu, O. Klein, M. Belmeguenai, Y. Roussigné, A. Stashkevich, S. M. Chérif, L. Aballe, M. Foerster, M. Chshiev, S. Auffret, I. M. Miron, and G. Gaudin, Room-temperature chiral magnetic skyrmions in ultrathin magnetic nanostructures, Nat. Nanotechnol. **11**, 449 (2016).
[11] H. Yang, A. Thiaville, S. Rohart, A. Fert, and M. Chshiev, Anatomy of Dzyaloshinskii-Moriya interaction at Co/Pt interfaces, Phys. Rev. Lett. **115**, 267210 (2015).
[12] S. Jenkins, W. J. Fan, R. Gaina, R. W. Chantrell, T. Klemmer, and R. F. L. Evans, Atomistic origin of exchange anisotropy in noncollinear γ-$IrMn_3$-CoFe bilayers, Phys. Rev. B **102**, 140404(R) (2020).
[13] S. Jenkins, R. W. Chantrell, T. J. Klemmer, and R. F. L. Evans, Magnetic anisotropy of the noncollinear antiferromagnet $IrMn_3$, Phys. Rev. B **100**, 220405(R) (2019).
[14] S. Jenkins, R. W. Chantrell, and R. F. L. Evans, Atomistic simulations of the magnetic properties of Ir_x Mn_{1-x} alloys, Phys. Rev. Mater. **5**, 034406 (2021).
[15] R. F. L. Evans, W. J. Fan, P. Chureemart, T. A. Ostler, M. O. A. Ellis, and R. W. Chantrell, Atomistic spin model simulations of magnetic nanomaterials, J. Phys.: Condens. Matter **26**, 103202 (2014).
[16] J. D. Alzate-Cardona, D. Sabogal-Suárez, R. F. L. Evans, and E. Restrepo-Parra, Optimal phase space sampling for Monte Carlo simulations of Heisenberg spin systems, J. Phys.: Condens. Matter **31**, 095802 (2019).
[17] J. L. García-Palacios and F. J. Lázaro, Langevin-dynamics study of the dynamical properties of small magnetic particles, Phys. Rev. B **58**, 14937 (1998).
[18] G. Vallejo-Fernandez, N. P. Aley, L. E. Fernandez-Outon, and K. O'Grady, Control of the setting process in CoFe/IrMn exchange bias systems, J. Appl. Phys. **104**, 033906 (2008).
[19] K. O'Grady, L. E. Fernandez-Outon, and G. Vallejo-Fernandez, A new paradigm for exchange bias in polycrystalline thin films, J. Magn. Magn. Mater. **322**, 883 (2010).
[20] S. Jenkins, R. W. Chantrell, and R. F. L. Evans, Exchange bias in multigranular noncollinear $IrMn_3$/CoFe thin films, Phys. Rev. B **103**, 014424 (2021).
[21] L. Szunyogh, B. Lazarovits, L. Udvardi, J. Jackson, and U. Nowak, Giant magnetic anisotropy of the bulk antiferromagnets IrMn and $IrMn_3$ from first principles, Phys. Rev. B **79**, 020403(R) (2009).

[22] X. Ma, G. Yu, S. A. Razavi, S. S. Sasaki, X. Li, K. Hao, S. H. Tolbert, K. L. Wang, and X. Li, Dzyaloshinskii-Moriya interaction across an antiferromagnet-ferromagnet interface, Phys. Rev. Lett. **119**, 027202 (2017).

[23] R. A. Khan, H. T. Nembach, M. Ali, J. M. Shaw, C. H. Marrows, and T. A. Moore, Magnetic domain texture and the Dzyaloshinskii-Moriya interaction in Pt/Co/IrMn and Pt/Co/FeMn thin films with perpendicular exchange bias, Phys. Rev. B **98**, 064413 (2018).

[24] V. Baltz, Thermally driven asymmetric responses of grains versus spin-glass related distributions of blocking temperature in exchange biased Co/IrMn bilayers, Appl. Phys. Lett. **102**, 062410 (2013).

[25] X. S. Wang, H. Y. Yuan, and X. R. Wang, A theory on skyrmion size, Commun. Phys. **1**, 31 (2018).

[26] B. Berg and M. Lüscher, Definition and statistical distributions of a topological number in the lattice O(3) σ-model, Nucl. Phys. B **190**, 412 (1981).

[27] M. Böttcher, S. Heinze, S. Egorov, J. Sinova, and B. Dupé, *B-T* phase diagram of Pd/Fe/Ir(111) computed with parallel tempering Monte Carlo, New J. Phys. **20**, 103014 (2018).

[28] J. Nogués and I. K. Schuller, Exchange bias, J. Magn. Magn. Mater. **192**, 203 (1999).

[29] A. Sakuma, K. Fukamichi, K. Sasao, and R. Y. Umetsu, First-principles study of the magnetic structures of ordered and disordered Mn-Ir alloys, Phys. Rev. B **67**, 024420 (2003).

[30] S. Jenkins and R. F. L. Evans, Enhanced finite size and interface mixing effects in iridium manganese ultra thin films, J. Appl. Phys. **124**, 152105 (2018).

[31] B. Jabakhanji and D. Ghader, Designing layered 2D skyrmion lattices in Moiré magnetic hetero-structures, arXiv:2302.01074.

[32] Y. Ga, D. Yu, L. Wang, P. Li, J. Liang, and H. Yang, Layer-dependent Dzyaloshinskii-Moriya interaction and field-free topological magnetism in two-dimensional Janus MnSTe, 2D Mater. **10**, 035020 (2023).

[33] H. Reichlová, V. Novák, Y. Kurosaki, M. Yamada, H. Yamamoto, A. Nishide, J. Hayakawa, H. Takahashi, M. Maryško, J. Wunderlich, X. Marti, and T. Jungwirth, Temperature and thickness dependence of tunneling anisotropic magnetoresistance in exchange-biased Py/IrMn/MgO/Ta stacks, Mater. Res. Express **3**, 076406 (2016).

[34] L. Šmejkal, Y. Mokrousov, B. Yan, and A. H. MacDonald, Topological antiferromagnetic spintronics, Nat. Phys. **14**, 242 (2018).

[35] D. Xiao, M.-C. Chang, and Q. Niu, Berry phase effects on electronic properties, Rev. Mod. Phys. **82**, 1959 (2010).

[36] B. Göbel, A. Mook, J. Henk, and I. Mertig, The family of topological Hall effects for electrons in skyrmion crystals, Eur. Phys. J. B **91** (2018).

[37] H. Chen, Q. Niu, and A. H. MacDonald, Anomalous Hall effect arising from noncollinear antiferromagnetism, Phys. Rev. Lett. **112**, 017205 (2014).

[38] L. Šmejkal, J. Sinova, and T. Jungwirth, Beyond conventional ferromagnetism and antiferromagnetism: A phase with nonrelativistic spin and crystal rotation symmetry, Phys. Rev. X **12**, 031042 (2022).

[39] S. Nakatsuji, N. Kiyohara, and T. Higo, Large anomalous Hall effect in a non-collinear antiferromagnet at room temperature, Nature (London) **527**, 212 (2015).

[40] Z. Feng, X. Zhou, L. Šmejkal, L. Wu, Z. Zhu, H. Guo, R. González-Hernández, X. Wang, H. Yan, P. Qin, X. Zhang, H. Wu, H. Chen, Z. Meng, L. Liu, Z. Xia, J. Sinova, T. Jungwirth, and Z. Liu, An anomalous Hall effect in altermagnetic ruthenium dioxide, Nat. Electron. **5**, 735 (2022).

[41] H. Reichlová, R. L. Seeger, R. González-Hernández, I. Kounta, R. Schlitz, D. Kriegner, P. Ritzinger, M. Lammel, M. Leiviskä, V. Petříček, P. Doležal, E. Schmoranzerová, A. Bad'ura, A. Thomas, V. Baltz, L. Michez, J. Sinova, S. T. B. Goennenwein, T. Jungwirth, and L. Šmejkal, Macroscopic time reversal symmetry breaking by staggered spin-momentum interaction, arXiv:2012.15651.

[42] J. Železný, Y. Zhang, C. Felser, and B. Yan, Spin-polarized current in noncollinear antiferromagnets, Phys. Rev. Lett. **119**, 187204 (2017).

[43] R. González-Hernández, L. Šmejkal, K. Výborný, Y. Yahagi, J. Sinova, T. Jungwirth, and J. Železný, Efficient electrical spin splitter based on nonrelativistic collinear antiferromagnetism, Phys. Rev. Lett. **126**, 127701 (2021).

[44] A. Bose, N. J. Schreiber, R. Jain, D.-F. Shao, H. P. Nair, J. Sun, X. S. Zhang, D. A. Muller, E. Y. Tsymbal, D. G. Schlom, and D. C. Ralph, Tilted spin current generated by the collinear antiferromagnet ruthenium dioxide, Nat. Electron. **5**, 267 (2022).

[45] J. Barker and O. A. Tretiakov, Static and dynamical properties of antiferromagnetic skyrmions in the presence of applied current and temperature, Phys. Rev. Lett. **116**, 147203 (2016).

[46] B. Göbel, A. Mook, J. Henk, and I. Mertig, Antiferromagnetic skyrmion crystals: Generation, topological Hall, and topological spin Hall effect, Phys. Rev. B **96**, 060406(R) (2017).

[47] C. A. Akosa, O. A. Tretiakov, G. Tatara, and A. Manchon, Theory of the topological spin Hall effect in antiferromagnetic skyrmions: Impact on current-induced motion, Phys. Rev. Lett. **121**, 097204 (2018).

[48] https://www.archer2.ac.uk.